Continuous Pulse-Density Modulation of Series-Resonant Converter for Wide-Range High-Resolution Output Voltage and High Efficiency

Zhijian Fang, *Member, IEEE*, Shizhao Liu, Rui Li, Yunfei Zhao, Li Fang, Han Cao, and Junhao Luo, *Member, IEEE*

***Abstract*—Pulse-density modulation (PDM) can achieve high efficiency in high-frequency dc–dc converters by implementing both zero-voltage-switching (ZVS) and zero-current-switching (ZCS). However, the discrete feature of pulse density, defined as the ratio of transferring energy switching cycles P to total switching cycles N, limits the voltage regulation flexibility. This article proposes a continuous pulse-density modulation (CPDM) for bidirectional series-resonant converter (BSRC). Compared to conventional PDM methods, this approach integrates a hybrid modulation comprising pulsewidth modulation and phase-shift modulation into one of the energy transfer switching cycles. The duty cycle is regulated to achieve continuous voltage regulation. The phase shift is controlled to ensure that the resonant current reaches zero at the end of the switching cycle, thereby enabling both ZVS and ZCS to be achieved during the remaining switching cycles. In addition, the converter achieves perfect load-independent output voltage and high-efficiency features, making it well-suited for a wide range of dc–dc converter applications. Finally, a 500 W BSRC prototype is constructed to verify the proposed CPDM. A high efficiency of 95% is achieved across the entire load range, along with continuous voltage regulation capability and load-independent characteristics.**

***Index Terms*—Bidirectional series-resonant converter (BSRC), continuous voltage regulation, load-independent voltage, pulse-density modulation (PDM).**

I. Introduction

BIDIRECTIONAL dc–dc converters, serving as the interface between the battery and grid-connected inverter, have drawn increasing attentions in recent years due to the rapid development of EV chargers and storage systems [1], [2], [3], [4], [5]. Given the wide voltage variation of batteries during charging or discharging, bidirectional dc–dc converters need to operate across a wide range. In addition, a high switching frequency is also desired to reduce the equipment volume and weight. However, a wide operation range and high switching frequency could degrade the converter's efficiency, leading to significant power losses and complicated thermal design, thus increasing costs. Achieving high efficiency and high frequency across the entire operation range presents a challenge for bidirectional dc–dc converters [6], [7].

The series-resonant converter is used for bidirectional dc–dc conversion, which is also named as bidirectional series-resonant converter (BSRC), but limited by its operating range. To extend the output range, a bidirectional LLC resonant converter is proposed in [8], [9], and [10], offering high efficiency and high switching frequency owing to its wide soft-switching range. However, the resonant tank's asymmetry may lead to a transition to LC series resonance when the power transfer is reversed. Subsequently, numerous symmetric resonant tanks have been introduced, such as $LLLC$ [11], $LCLC$ [12], LCL [13], among others. However, the bulky tank could increase costs and lead to significant circulating currents. Therefore, the BSRC is proposed [14], [15], [16], [17], employing an LC series resonant tank, which is symmetric and simpler, thus reducing costs and enhancing efficiency.

Since BSRC can be regarded as resonant versions of the famous dual active bridge (DAB) converter, pase-shift modulations (PSMs) can be used for the BSRC. Single-phase-shift modulation, a traditional control method for DAB converters, regulates the outer phase shift between the input and output bridges. Despite simple implementation, it suffers from a limited ZVS range and reduced efficiency. To overcome these limitations, an additional degree of freedom is introduced by incorporating the inner phase shift, resulting in dual phase shift [7], [18] and extended phase-shift modulations [19]. When both inner phase shifts of the input/output bridges can be adjusted independently, triple phase-shift modulation [20] is achieved.

Despite the PSM [21], [22] could achieve wide operating range, soft-switching losing and large circulating currents result in significant power losses. To extend the soft-switching range, pulse-frequency modulation (PFM) is employed in BSRCs [23],

Received 9 May 2024; revised 15 July 2024 and 26 September 2024; accepted 31 October 2024. Date of publication 7 November 2024; date of current version 26 December 2024. This work was supported in part by the Key Research and Development Program of Hubei Province under Grant 2023BAB082. Recommended for publication by Associate Editor O. Lucia. *(Corresponding author: Junhao Luo.)*

Zhijian Fang and Yunfei Zhao are with the School of Automation, China University of Geosciences, Wuhan 430074, China (e-mail: fangzj@cug.edu.cn; 20191001422@cug.edu.cn).

Rui Li, Li Fang, and Han Cao are with the Wuhan Second Ship Design and Research Institute, Wuhan 430064, China (e-mail: d201077271@alumni.hust.edu.cn; FangLi1995@whu.edu.cn; wangtianzheng@mail.iee.ac.cn).

Shizhao Liu is with the School of Electronics and Electrical Engineering, Wuhan Textile University, Wuhan 430073, China (e-mail: liushizhao.tony@megmeet.com).

Junhao Luo is with the Analog Devices Inc., Wilmington, MA 01887 USA (e-mail: luo.ju@northeastern.edu).

Color versions of one or more figures in this article are available at https://doi.org/10.1109/TPEL.2024.3493895.

Digital Object Identifier 10.1109/TPEL.2024.3493895

[24]. However, the flat curve of gain versus frequency renders it nearly impossible to adjust the wide battery voltage range. To address large circulating currents, pulsewidth modulation (PWM) is introduced into the inverter or rectifier bridges of the BSRC to mitigate the circulating power loss induced by PSM [25], [26]. However, soft switching may be compromised, particularly under light load conditions. To preserve all the advantages, PFM is integrated with PSM to attain soft switching while accommodating a wide range [27]. Nevertheless, achieving soft switching necessitates a large circulating current, which reduces efficiency. In [28] and [29], a hybrid modulation scheme incorporating PFM, PSM, and PWM is proposed to enhance the efficiency of BSRC across a broad power and gain range. However, the use of fundamental approximations leads to inaccurate optimal results, and complex calculations pose challenges to implementation.

To address these challenges, sinusoidal modulation is employed to control the BSRC at a fixed resonant frequency [30], [31], enabling soft switching and unidirectional power flow to achieve high efficiency. However, this approach fixes the voltage gain and lacks control over power. Recently, pulse-density modulation (PDM) has been proposed, which regulates the output power by adjusting the duration of energy transmission to the load within a fixed control period. By fixing the switching frequency to the resonant frequency during the transmission period, sinusoidal currents can be achieved, enabling both zero-voltage-switching (ZVS) and zero-current-switching (ZCS), thereby achieving high efficiency over a wide operating range [32], [33]. However, significant power fluctuation occurs in PDM due to the long control period, leading to increased filter stress and reduced efficiency.

An enhanced PDM (EPDM) is proposed in [34] to reduce the power fluctuations. The original switching cycle is divided into two subperiods to distribute the transmitted energy. However, the presence of a dc component in the output voltage can lead to unbalanced switching and increased conduction losses in the switches. An improved pulse-density modulation (IPDM) is introduced to optimize the distribution of switch sequences and minimize power fluctuations [35]. However, the discrete feature of pulse density, defined as the ratio of energy-transferring switching cycles P to total switching cycles N, poses challenges to voltage regulation in all PDM methods. Unfortunately, batteries are highly sensitive to voltage fluctuations, as even slight overcharging can cause irreversible damage. Therefore, accurate voltage regulation is crucial in battery charging or discharging applications, which presents a challenge to PDM methods.

To address the traditional PDM issues, a continuous pulse-density modulation (CPDM) is proposed for BSRC in this article. A hybrid modulation incorporating PWM and PSM is introduced into one of the energy-transferring switching cycles in traditional PDM. The duty cycle is regulated to achieve continuous voltage regulation. The phase shift is controlled to ensure that the resonant current reaches zero at the end of each switching cycle, thereby enabling both ZVS and ZCS to be achieved during the remaining switching cycles. In addition, the proposed method achieves perfect load-independent output voltage and high efficiency features, making it suitable for a wide range of dc–dc converter applications.

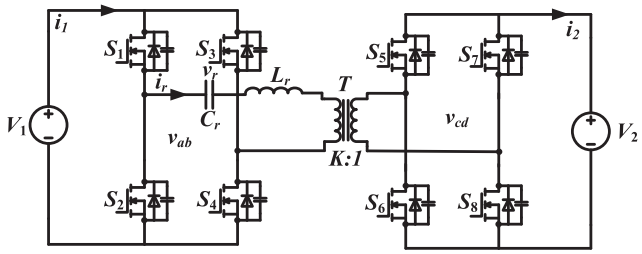

Fig. 1. Schematics of the BSRC.

The comparison between the proposed CPDM and traditional methods is presented in Table I. Compared to traditional methods, the contributions of the proposed method are summarized as follows.

1) The proposed CPDM achieves a wide output voltage and load range. Theoretically, the output voltage can be controlled from zero to V_1/K. In addition, the output voltage is independent of the load, resulting in a wide load range.
2) The proposed CPDM achieves both zero-voltage ZCS (ZVZCS) and nonbackflow power over a wide range, resulting in high efficiency across a wide load range.
3) High-resolution voltage can be achieved even with a small control period N, as continuous voltage regulation is realized by the proposed CPDM, thereby reducing power fluctuations.

The rest of this article is organized as follows. Section II provides an introduction to both traditional PDM and the proposed CPDM, along with their corresponding waveforms and phase plane trajectories. The operation analysis and the corresponding mathematical description of the CPDM are given in Section III. In Section IV, the characteristic analysis is presented. Section V discusses the experiments conducted to verify the proposed modulation. Finally, Section VI concludes this article.

II. Proposed Method

The structure diagram of the BSRC is shown in Fig. 1. V_1 and V_2 are the input and output voltage, respectively. i_1 and i_2 are the input and output current, respectively. The terminal voltages of the inverter and rectifier bridges, labeled as $v_{\rm ab}$ and $v_{\rm cd}$, consist of four MOSFETs, namely S_1–S_4 and S_5–S_8, respectively. $L_{\rm r}$ and $C_{\rm r}$ are the resonant inductor and capacitor, forming the series resonant tank. $i_{\rm r}$ represents the resonant current flowing through the resonant tank, while $v_{\rm r}$ signifies the resonant voltage across $C_{\rm r}$. In addition, a high-frequency transformer T with a turn ratio of K connects with the resonant tank and rectifier bridges.

A. Conventional PDM

In the conventional PDM, the resonant period $T_{\rm r}$ reflects the switching cycle, allowing for ZVS-ON and ZCS-OFF of the switches. In addition, a control period of PDM, denoted as $T_{\rm all}$, consists of N resonant periods $T_{\rm r}$. As shown in Fig. 2, $T_{\rm all}$ is divided into two parts: the transmitting period $T_{\rm on}$ with

TABLE I
COMPARISON OF MODULATION SCHEMES FOR BSRC

Methodology	Operating range	Soft switching	Backflow power	Efficiency of light load	Efficiency of full load	Input / Output voltage	Power	Regulation ability	Power ripple
PFM [23], [24]	Narrow	ZVS-ON, hard-OFF	Medium	86%	95%	400V/ 24V - 48V	480W	Nonlinear, continuous	Small
PSM [21], [22]	Wide	ZVS-ON, hard-OFF	Large	82%	95%	20V/ 20V	40W	Nonlinear, continuous	Small
PSM+PWM [25], [26]	Wide	ZVS-ON, hard-OFF	Small	83%	95%	500V/ 400V	1kW	Nonlinear, continuous	Small
PSM+PFM [27]	Wide	ZVS-ON, hard-OFF	Medium	95.5%	88%	200V/ 100V - 200V	800W	Nonlinear, continuous	Small
PSM+PWM+PFM [28], [29]	Wide	ZVS-ON, hard-OFF	Small	95%	90%	195V - 250V/ 24V - 48V	1kW	Nonlinear, continuous	Small
PDM [32], [33]	Wide	ZVS-ON, ZCS-OFF	None	86%	95%	500V/ 480V	100kW	Linear, discrete	Large
EPDM [34]	Wide	ZVS-ON, ZCS-OFF	None	90%	95%	500V/ 480V	100kW	Linear, discrete	Medium
IPDM [35]	Wide	ZVS-ON, ZCS-OFF	None	80%	88%	300V/ 300V	20kW	Linear, discrete	Medium
Proposed CPDM	Wide	ZVS-ON, ZCS-OFF	None	94.5%	96.1%	200V/ 100V - 200V	500W	Linear, continuous	Small

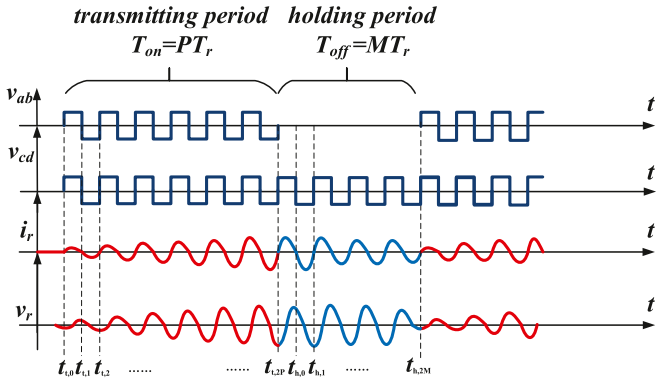

Fig. 2. Resonant voltage and current waveforms of conventional PDM.

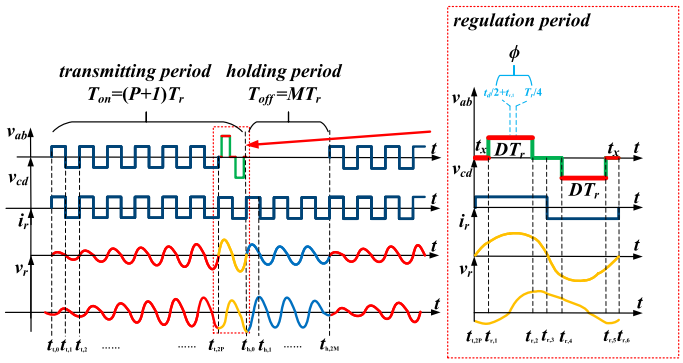

Fig. 3. Resonant voltage and current waveforms of CPDM.

P switching cycles $T_{\rm r}$ and the holding period $T_{\rm off}$ with M switching cycles $T_{\rm r}$. In the transmitting period $T_{\rm on}$, the inverter bridges operate at the resonant frequency f_r, generating sinusoidal waveforms of $i_{\rm r}$ and $v_{\rm r}$.The power is delivered from the input to the output, with $i_{\rm r}$ in phase with $v_{\rm r}$, achieving ZVS-ON and ZCS-OFF. Conversely, during the holding period $T_{\rm off}$, the inverter bridges supply a zero-level voltage of $v_{\rm ab}$, resulting in no power transmission. Consequently, the output voltage is determined by the pulse density, defined as P/N.

Since the number P, N, and M are integers, the pulse density is discrete in conventional PDM, preventing step-less adjustment.The resolution of PDM is determined by N. A larger N improves voltage regulation accuracy. For example, to achieve a voltage accuracy of less than 0.1% in an EV charger, the total number of switching cycles within one control period N should exceed 1000. However, a large N can lead to significant power fluctuations and voltage ripples. Various optimal design methods have been proposed to select an appropriate N or distribute the switching sequence to balance high accuracy and minimal power fluctuations. Nevertheless, pulse density remains discrete in all optimal PDM methods, preventing the implementation of step-less regulation. Therefore, improving conventional PDM to achieve continuous voltage gain is necessary to meet the high-accuracy requirement of battery charge or discharge.

B. Proposed CPDM

To improve the voltage regulation accuracy, a CPDM is proposed in this article. PWM is introduced into one of the switching cycles for voltage control, as illustrated in Fig. 3. The CPDM control period consists of three stages. Stages 1 and 3 represent the transmitting period $T_{\rm on}$ and holding period $T_{\rm off}$, respectively, are identical to conventional PDM. In the additional Stage 2, the duty cycle of the resonant period can be continuously regulated to control the voltage gain between P/N and $(P+1)/N$. Consequently, high-voltage accuracy can be achieved even with a small value of N. For instance, with a minimum duty cycle of approximately 0.01, a voltage accuracy of 0.1% can be attained with $N=10$, reducing the power ripples as well. In essence, the introduction of PWM changes the transmitting period from an integral P to a floating value $P+\sin(D\pi)$, thereby ensuring continuous pulse density and enabling step-less adjustment.

During Stage 2, the initial and final values of resonant current $i_{\rm r}$ should be zero. Otherwise, $i_{\rm r}$ and terminal voltage $v_{\rm ab}$ become out-of-phase, leading to hard switching and significant reactive power during Stages 1 and 3. Therefore, PSM must be employed to control the duty cycle phase $t_{\rm x}$ and achieve zero resonant current $i_{\rm r}$ for variable duty cycle at the beginning and end of Stage 2. This ensures that the remarkable characteristics of conventional PDM, specifically ZVZCS and nonbackflow power, are preserved by the proposed CPDM.

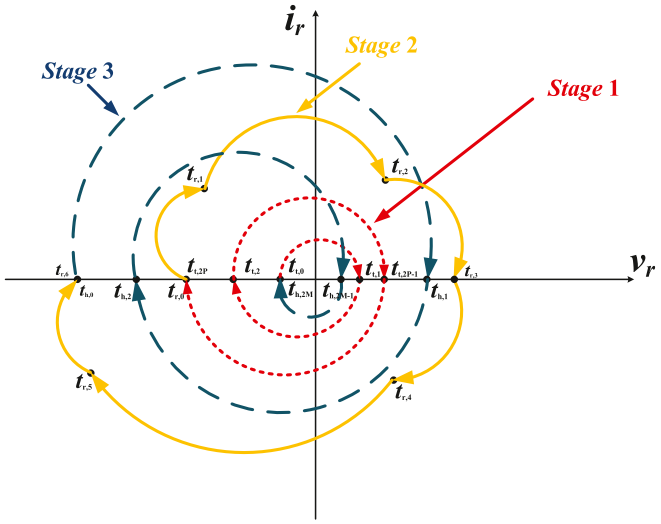

Fig. 4. Trajectory diagram of conventional CPDM with i_r versus v_r.

III. Operation Analysis of CPDM

In Fig. 3, the proposed CPDM is divided into three stages. The operation analysis of each stage is provided below. To clearly express the operation, the trajectory curve of CPDM with i_r versus v_r is also depicted in Fig. 4.

A. Stage 1: Transmitting Period

In stage 1, the transmitting period T_{on} comprises P switching cycles, fixed to the resonant period, i.e., $T_{on} = PT_r$. In each switching cycle, the inverter and rectifier bridges are controlled to provide a square waveform with duty cycle of 0.5, generating sinusoidal resonant current. $t_{t,i}$ denotes the switching time of each switch and $v_{r,ti}$ is the instantaneous value of v_r at $t_{t,i}$, where $i = 0, 1, 2, \ldots, 2P$. As the switching frequency equals the resonant frequency, $t_{t,i} = \frac{i}{2}T_r$.

1) $t_{t,0}$–$t_{t,1}$: S_1, S_4 and S_5, S_8 are ON while the other switches are OFF, resulting in $v_{ab} = V_1$ and $v_{cd} = V_2$. V_1 charges V_2 through the resonant tank. Then, the state equations can be written as

$$L_r \frac{di_r}{dt} + v_r = v_{eq} \tag{1}$$

$$C_r \frac{dv_r}{dt} = i_r \tag{2}$$

where v_{eq} is the equivalent voltage, calculated as $V_1 - KV_2$. Owing to the sinusoidal resonant current i_r, i_r is zero at $t_{t,ti}$. i_r and v_r can be derived

$$i_r = \frac{v_{eq} - v_{r,t0}}{Z_r} \sin(\omega_r t) \tag{3}$$

$$v_r = -(v_{eq} - v_{r,t0}) \cos(\omega_r t) + v_{eq} \tag{4}$$

where ω_r is resonant angular frequency and Z_r is characteristic impedance, as defined in the following equation:

$$\omega_r = 2\pi f_r = \frac{1}{\sqrt{L_r C_r}} \tag{5}$$

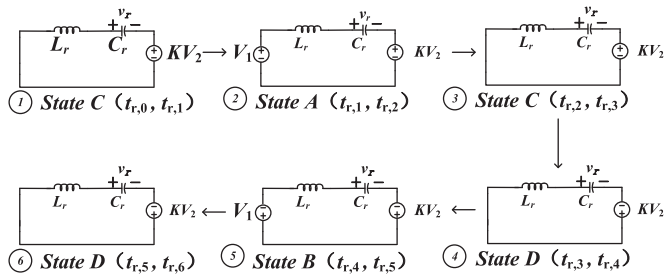

Fig. 5. Equal circuit of six states during the regulation period.

$$Z_r = \sqrt{\frac{L_r}{C_r}}. \tag{6}$$

Combining (3) and (4), the resonant current and voltage can be rewritten as

$$(i_r Z_r)^2 + (v_r - v_{eq})^2 = (v_{eq} - v_{r,t0})^2. \tag{7}$$

The phase trajectory diagram of i_r versus v_r forms a circle with a center at $(0, v_{eq})$ and a radius of $v_{eq} - v_{r,t0}$. At the end of this period, i_r could reach zero again and v_r changes to

$$v_{r,t1} = 2v_{eq} - v_{r,t0}. \tag{8}$$

2) $t_{t,1}$–$t_{t,2}$: During this period, S_2, S_3 and S_6, S_7 are ON while the other switches are OFF. v_{ab} and v_{cd} reverse to $-V_1$ and $-V_2$. Similar to the previous period, i_r and v_r can be derived

$$i_r = \frac{-v_{eq} - v_{r,t1}}{Z_r} \sin[\omega_r(t - t_{t,1})] \tag{9}$$

$$v_r = (v_{eq} + v_{r,t1}) \cos[\omega_r(t - t_{t,1})] - v_{eq}. \tag{10}$$

The center and radius of the trajectory curve circle changes to $(0, -v_{eq})$ and $-v_{eq} - v_{r,t1}$. v_r at $t_{t,t2}$ is

$$v_{r,t2} = -4v_{eq} + v_{r,t0}. \tag{11}$$

Similarly, the remaining equations for i_r and v_r can be obtained as shown in Fig. 4. The instantaneous values of v_r at each time can be derived as follows:

$$v_{r,ti} = \begin{cases} -2iv_{eq} + v_{r,t0}, & i \text{ is even} \\ 2iv_{eq} - v_{r,t0}, & i \text{ is odd.} \end{cases} \tag{12}$$

At the end of stage 1, i_r could reach zero again at $t_{t,2P}$ and v_r is

$$v_{r,t2P} = -4Pv_{eq} + v_{r,t0}. \tag{13}$$

B. Stage 2: Regulation Period

In stage 2, the regulation period is fixed to T_r. The duty cycle D and shifting phase ϕ are regulated to control the voltage and maintain ZVZCS. The total period can be divided into six states, as illustrated in Fig. 5. The detail analysis of each state is presented as follows.

1) $t_{t,2P}$–$t_{r,1}$: During this period, S_1, S_3 and S_5, S_8 are ON while the other switches are OFF, resulting in $v_{ab} = 0$ and $v_{cd} = V_2$. Then, i_r and v_r can be derived as

$$i_r = \frac{-KV_2 - v_{r,t2P}}{Z_r} \sin[\omega_r(t - t_{t,2P})] \tag{14}$$

$$v_{\mathrm{r}} = (KV_2 + v_{\mathrm{r,\,t2P}})\cos[\omega_{\mathrm{r}}(t - t_{\mathrm{t,\,2P}})] - KV_2. \tag{15}$$

At the end of this period, the instantaneous values of i_{r} and v_{r} can be obtained as

$$i_{\mathrm{r,\,r1}} = \frac{-KV_2 - v_{\mathrm{r,\,t2P}}}{Z_{\mathrm{r}}}\sin(\omega_{\mathrm{r}} t_{\mathrm{x}}) \tag{16}$$

$$v_{\mathrm{r,\,r1}} = (KV_2 + v_{\mathrm{r,\,t2P}})\cos(\omega_{\mathrm{r}} t_{\mathrm{x}}) - KV_2 \tag{17}$$

where $t_{\mathrm{x}} = t_{\mathrm{r,\,1}} - t_{\mathrm{t,\,2P}}$.

2) $t_{\mathrm{r,\,1}}$–$t_{\mathrm{r,\,2}}$: S_3 is OFF while S_4 turns ON, then $v_{\mathrm{ab}} = V_1$. Similarly, i_{r} and v_{r} can be given as

$$\begin{aligned} i_{\mathrm{r}} = {} & \frac{v_{\mathrm{eq}} - v_{\mathrm{r,\,r1}}}{Z_{\mathrm{r}}}\sin[\omega_{\mathrm{r}}(t - t_{\mathrm{r,\,1}})] \\ & + i_{\mathrm{r,\,r1}}\cos[\omega_{\mathrm{r}}(t - t_{\mathrm{r,\,1}})] \end{aligned} \tag{18}$$

$$\begin{aligned} v_{\mathrm{r}} = {} & -(v_{\mathrm{eq}} - v_{\mathrm{r,\,r1}})\cos[\omega_{\mathrm{r}}(t - t_{\mathrm{r,\,1}})] \\ & + Z_{\mathrm{r}} i_{\mathrm{r,\,r1}}\sin[\omega_{\mathrm{r}}(t - t_{\mathrm{r,\,1}})] + v_{\mathrm{eq}}. \end{aligned} \tag{19}$$

Then, $i_{\mathrm{r,\,r2}}$ and $v_{\mathrm{r,\,r2}}$ can be derived as

$$i_{\mathrm{r,\,r2}} = \frac{v_{\mathrm{eq}} - v_{\mathrm{r,\,r1}}}{Z_{\mathrm{r}}}\sin(\omega_{\mathrm{r}} t_{\mathrm{d}}) + i_{\mathrm{r,\,r1}}\cos(\omega_{\mathrm{r}} t_{\mathrm{d}}) \tag{20}$$

$$v_{\mathrm{r,\,r2}} = -(v_{\mathrm{eq}} - v_{\mathrm{r,\,r1}})\cos(\omega_{\mathrm{r}} t_{\mathrm{d}}) + Z_{\mathrm{r}} i_{\mathrm{r,\,r1}}\sin(\omega_{\mathrm{r}} t_{\mathrm{d}}) + v_{\mathrm{eq}}. \tag{21}$$

where $t_{\mathrm{d}} = t_{\mathrm{r,\,2}} - t_{\mathrm{r,\,1}}$.

3) $t_{\mathrm{r,\,2}}$–$t_{\mathrm{r,\,3}}$: S_1 is OFF while S_2 turns ON, then $v_{\mathrm{ab}} = 0$. The state equation is similar to that in the period from $t_{\mathrm{t,\,2P}}$ to $t_{\mathrm{r,\,1}}$. The ending time is half of the switching cycle, i.e., $t_{\mathrm{r,\,3}} - t_{\mathrm{t,\,2P}} = T_{\mathrm{r}}/2$. Then, $i_{\mathrm{r,\,r3}}$ and $v_{\mathrm{r,\,r3}}$ are given as

$$\begin{aligned} i_{\mathrm{r,\,r3}} = {} & \frac{-KV_2 - v_{\mathrm{r,\,r2}}}{Z_{\mathrm{r}}}\sin\omega_{\mathrm{r}}(t_{\mathrm{x}} + t_{\mathrm{d}}) \\ & - i_{\mathrm{r,\,r2}}\cos\omega_{\mathrm{r}}(t_{\mathrm{x}} + t_{\mathrm{d}}) \end{aligned} \tag{22}$$

$$\begin{aligned} v_{\mathrm{r,\,r3}} = {} & -(KV_2 + v_{\mathrm{r,\,r2}})\cos\omega_{\mathrm{r}}(t_{\mathrm{x}} + t_{\mathrm{d}}) \\ & + Z_{\mathrm{r}} i_{\mathrm{r,\,r2}}\sin\omega_{\mathrm{r}}(t_{\mathrm{x}} + t_{\mathrm{d}}) - KV_2. \end{aligned} \tag{23}$$

Specially, i_{r} should reach zero at t_{r3}. t_{x} should be optimally design to ensure that $i_{\mathrm{r,\,r3}} = 0$ for variable t_{d}. The duty cycle D and shifting phase ϕ are define as

$$D = \frac{t_{\mathrm{d}}}{T_{\mathrm{r}}} \tag{24}$$

$$\phi = \omega_{\mathrm{r}}\left(\frac{t_{\mathrm{d}}}{2} + t_{\mathrm{x}}\right) - \frac{\pi}{2}. \tag{25}$$

Combining (14) to (25), the critical conditions for $i_{\mathrm{r,\,r3}} = 0$ are derived as

$$t_{\mathrm{x}} = \frac{T_{\mathrm{r}}}{4} - \frac{t_{\mathrm{d}}}{2} \tag{26}$$

$$\phi = 0. \tag{27}$$

Noticeably, the phase shift ϕ is set to zero during the regulation period regardless of the duty cycle D. There is no need to use the closed-loop regulation to control the phase shift angle. The CPDM can be simply implemented.

Then, the instantaneous values of i_{r} and v_{r} at each time can be calculated

$$v_{\mathrm{r,\,r1}} = a\sin\left(\frac{\omega_{\mathrm{r}} t_{\mathrm{d}}}{2}\right) - KV_2 \tag{28}$$

$$v_{\mathrm{r,\,r2}} = 2V_1\sin^2\left(\frac{\omega_{\mathrm{r}} t_{\mathrm{d}}}{2}\right) - a\sin\left(\frac{\omega_{\mathrm{r}} t_{\mathrm{d}}}{2}\right) - KV_2 \tag{29}$$

$$v_{\mathrm{r,\,r3}} = 2V_1\sin\left(\frac{\omega_{\mathrm{r}} t_{\mathrm{d}}}{2}\right) - a - KV_2 \tag{30}$$

$$i_{\mathrm{r,\,r1}} = -\frac{a}{Z_{\mathrm{r}}}\cos\left(\frac{\omega_{\mathrm{r}} t_{\mathrm{d}}}{2}\right) \tag{31}$$

$$i_{\mathrm{r,\,r2}} = \frac{V_1}{Z_{\mathrm{r}}}\sin(\omega_{\mathrm{r}} t_{\mathrm{d}}) - \frac{a}{Z_{\mathrm{r}}}\cos\left(\frac{\omega_{\mathrm{r}} t_{\mathrm{d}}}{2}\right) \tag{32}$$

$$i_{\mathrm{r,\,r3}} = 0 \tag{33}$$

where $a = KV_2 + v_{\mathrm{r,\,t2P}}$.

Similarly, the instantaneous values of i_{r} and v_{r} at the remaining time can be obtained as

$$v_{\mathrm{r,\,r4}} = 2V_1\sin^2\frac{\omega_{\mathrm{r}} t_{\mathrm{d}}}{2} - (2KV_2 + a)\sin\frac{\omega_{\mathrm{r}} t_{\mathrm{d}}}{2} + KV_2 \tag{34}$$

$$v_{\mathrm{r,\,r5}} = 2V_1(\cos\omega_{\mathrm{r}} t_{\mathrm{d}} - 1) + KV_2 + (2KV_2 + a)\sin\frac{\omega_{\mathrm{r}} t_{\mathrm{d}}}{2} \tag{35}$$

$$v_{\mathrm{r,\,r6}} = -4V_1\sin\frac{\omega_{\mathrm{r}} t_{\mathrm{d}}}{2} + 4KV_2 + v_{\mathrm{r,\,t2P}} \tag{36}$$

$$i_{\mathrm{r,\,r4}} = \frac{(2KV_2 + a)\cos\frac{\omega_{\mathrm{r}} t_{\mathrm{d}}}{2} - V_1\sin\omega_{\mathrm{r}} t_{\mathrm{d}}}{Z_{\mathrm{r}}} \tag{37}$$

$$i_{\mathrm{r,\,r5}} = \frac{-2V_1\sin\omega_{\mathrm{r}} t_{\mathrm{d}} + (2KV_2 + a)\cos\frac{\omega_{\mathrm{r}} t_{\mathrm{d}}}{2}}{Z_{\mathrm{r}}} \tag{38}$$

$$i_{\mathrm{r,\,r6}} = 0. \tag{39}$$

C. Stage 3: Holding Period

In stage 3, the holding period T_{off} consists of M switching cycles, denoted as $T_{\mathrm{off}} = MT_{\mathrm{r}}$. During this period, the inverter bridge maintains a fixed zero level, while the rectifier bridge is modulated with resonant period and a duty cycle of 0.5. $t_{\mathrm{h,\,i}}$ denotes the switching time of each switch and $v_{\mathrm{r,\,hi}}$ represents the instantaneous value of v_{r} at $t_{\mathrm{h,\,i}}$ where $i = 1, 2, \ldots, 2M$.

The operation of stage 3 is similar to stage 1. The instantaneous values of v_{r} at each time can be derived as follows.

$$v_{\mathrm{r,\,hi}} = \begin{cases} 2iKV_2 + v_{\mathrm{r,\,r6}}, & i \text{ is even} \\ -2iKV_2 - v_{\mathrm{r,\,r6}}, & i \text{ is odd.} \end{cases} \tag{40}$$

At the end of stage 3, i_{r} could reach zero again at $t_{\mathrm{h,\,2M}}$ and v_{r} is

$$v_{\mathrm{r,\,h2M}} = 4MKV_2 + v_{\mathrm{r,\,r6}}. \tag{41}$$

According to the abovementioned operation analysis, it can be observed that the power characteristics of the BSRC with CPDM are determined by the initial value of v_{r}, which varies with the pulse density $\frac{P}{N}$ and duty cycle D. Consequently, the output power can be controlled by regulating $\frac{P}{N}$ and D. In addition, the

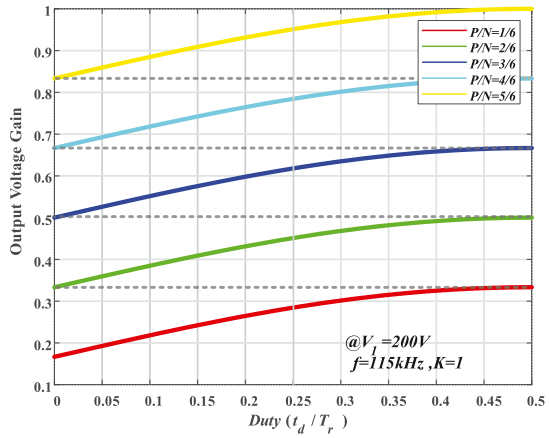

Fig. 6. Curves of output voltage gain KV_2/V_1 versus D with different P.

shifting phase ϕ during the regulation period should be set to zero to ensure ZVZCS during both the transmitting and holding periods.

IV. Feature Analysis

A. Output Voltage

Since the resonant current $i_{\rm r}$ and voltage $v_{\rm r}$ are continuous throughout the entire control period, (42) can be obtained

$$v_{\rm r,\,h2M} = v_{\rm r,\,t0}. \tag{42}$$

Then, the output voltage can be derived based on the analysis in Section III

$$V_2 = \frac{P + \sin\frac{\omega_{\rm r} t_{\rm d}}{2}}{K(1+M+P)} V_1 = \frac{P+\sin(D\pi)}{KN} V_1 \tag{43}$$

where N is the total switching cycles in a control period, given by $P+M+1$. Compared to the conventional PDM, the discreted pulse density $\frac{P}{N}$ is transformed into a continuous function $\frac{P+\sin(D\pi)}{N}$. The transmitting period P determines the approximate range of the output voltage V_2. Then, V_2 can be continuously and precisely controlled by regulating the duty cycle D within the gain range from $\frac{P}{N}$ to $\frac{P+1}{N}$. The proposed CPDM allows for a wide gain range from 0 to 1.

Fig. 6 presents curves illustrating the output voltage gain KV_2/V_1 as a function of duty cycle D for various values of P. As the duty cycle D varies from 0 to 0.5, the gain range almost linearly increases from $\frac{P}{N}$ to $\frac{P+1}{N}$. In addition, when D is regulated to 0.5, the regulation period may transfer to a resonant switching cycle, resulting in an automatic increase from $\frac{P+\sin(D\pi)}{N}$ to $\frac{P+1}{N}$. Therefore, the voltage gain could continuously vary across different regions.

The output voltage V_2 remains independent of the load, achieving constant output voltage, which is a crucial attribute for battery charging or discharging applications. Based on the operation analysis in section III, the output current can be derived as

$$i_2 = \frac{2}{\pi Z_{\rm r}}\left[-v_{\rm r,\,t0} + 2\frac{P(M+1)+(M-P)\sin(D\pi)}{N} V_1\right]. \tag{44}$$

The output current is determined by the load and the initial value of $v_{\rm r,\,t0}$.

B. Soft Switching

The outstanding feature of PDM is ZVZCS for all switches. In conventional PDM methods, the switching frequency $f_{\rm s}$ is fixed to resonant frequency $f_{\rm r}$, aligning the resonant current $i_{\rm r}$ in phase with the terminal voltage $v_{\rm ab}$ and $v_{\rm cd}$, thereby achieving ZVZCS for all switches. In CPDM, PWM is introduced for continuous output voltage regulation, but this may result in the loss of soft switching. To address this issue, the initial resonant currents $i_{\rm r,\,t0}$ and $i_{\rm r,\,r6}$, should be zero, which can be achieved when $\phi = 0$ according to the analysis in section III. In summary, the critical conditions for achieving soft switching in CPDM can be concluded as follows.

1) $f_{\rm s}$ is fixed to $f_{\rm r}$.
2) ϕ of duty cycle in the regulation period is set to zero.

Then, the terminal voltages reverse at the zero current crossing time, realizing ZVZCS.

In addition, because of parasitic capacitance and dead time, ZVZCS can only be achieved when the load is sufficiently large. The dead time $t_{\rm dead}$ of the switches should be adjusted to ensure that the current remains consistently positive or negative as the terminal voltage transitions from V_1 (or $-V_1$) to $-V_1$ (or V_1). According to [35], the critical condition can be given as

$$t_{\rm dead} > \frac{1}{\omega_{\rm r}} \cos^{-1}\left(1 - \frac{2\omega_{\rm r} C_{\rm e} V_1}{I_{\rm peak}}\right) \tag{45}$$

where $C_{\rm e}$ is the equivalent parasitic capacitance of switches and $I_{\rm peak}$ is the peak value of resonant current.

When the load is light, the resonant current i_r is zero when the terminal voltage reverses. Consequently, both ZCS-ON and ZCS-OFF are achieved by the switches, as noted in [5]. The resulting switching loss is minimal compared to other losses and can be considered negligible.

Specially, hard switching occurs for S_1 to S_4 in stage 2 (regulation period). However, since the hard switching loss only occurs in one switching cycle. As a result, the average switching loss over the entire control period could be almost negligible.

C. Loss Analysis

The power loss of BSRC using CPDM consists of five components: switch loss $P_{\rm S}$, transformer loss $P_{\rm T}$, inductor loss $P_{\rm Lr}$, capacitor loss $P_{\rm C}$, and other losses $P_{\rm Oth}$. The detailed losses calculation are listed in the Appendix.

Due to soft switching, the switching losses can be ignored. The conduction loss, determined by the RMS value of resonance current $I_{\rm rms}$, is the primary factor affecting efficiency. To evaluate the conduction loss of the converter, a ratio k_{ii} is defined

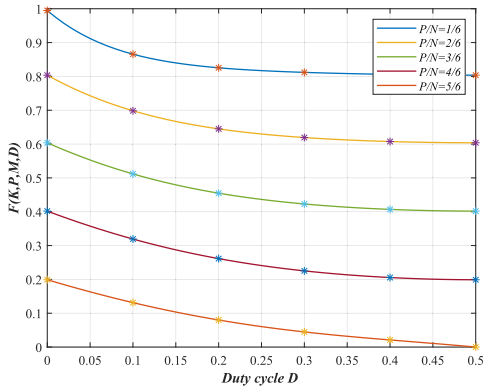

Fig. 7. Curves of $F(K, P, M, D)$ versus D with different P/N.

as

$$k_{ii} = \frac{I_{\rm rms}}{i_2} = \sqrt{F(K,P,M,D) \cdot \frac{R^2}{{Z_{\rm r}}^2} + \frac{\pi^2}{8}} \tag{46}$$

where $F(K, P, M, D)$ is a function of P, M, D, and K, as shown in Fig. 7. When the duty cycle D is increased from 0 to 0.5, $F(K, P, M, D)$ decreases. A higher P/N can result in a lower $F(K, P, M, D)$, thereby reducing the conduction loss.

$F(K, P, M, D)$ is typically very small, usually less than 1. In addition, the characteristic impedance Z_r is designed to be significantly larger than the load resistor R. Consequently, the influence of the duty cycle can be ignored. $I_{\rm rms}$ can be approximately derived as

$$I_{\rm rms} = k_{ii} i_2 \approx \frac{\pi}{2\sqrt{2}} i_2 \tag{47}$$

where i_2 is the average absolute value of resonant current $i_{\rm r}$. The relationship between the rms current and the average current of the proposed CPDM is almost equivalent to that in sinusoidal currents. This result proves that the proposed method minimizes conduction loss.

Based on the abovementioned analysis, the total power loss of the proposed BSRC is given by

$$\begin{aligned} P_{\rm Loss} &= P_{\rm S} + P_T + P_{Lr} + P_{\rm C} + P_{\rm Oth} \\ &= {I^2}_{\rm rms} r_{\rm total} + P_{\rm T,\,core} + P_{\rm Lr,\,core} \end{aligned}$$

where $r_{\rm total}$ is the total loss resistance, expressed as

$$r_{\rm total} = (2r_{\rm d} + 2K^2 r_{\rm s} + r_{\rm C} + r_T + r_{\rm oth} + r_{Lr}). \tag{48}$$

Due to nearly full soft switching and low $I_{\rm rms}$, minimal switching and conduction loss can be achieved, resulting in high efficiency. In addition, $I_{\rm rms}$ is linearly proportional to the output current i_2 and core loss remains constant and negligible. Therefore, the efficiency can be expressed as

$$\eta = \frac{V_2 i_2}{V_2 i_2 + P_{\rm Loss}} \approx \frac{V_2 i_2}{k_{ii}^2 i_2^2 r_{\rm total} + V_2 i_2} = \frac{V_2}{k_{ii}^2 i_2 r_{\rm total} + V_2} \tag{49}$$

where $k_{ii} = \frac{\pi}{2\sqrt{2}}$. The efficiency slightly decreases with increasing output power. High and nearly constant efficiency can be achieved.

TABLE II
PARAMETERS OF THE BSRC

Parameters	Symbols	Values
Primary-side switches	S_1–S_4	C3M0065090D
Secondary-side switches	S_5–S_8	C3M0065090D
Resonant inductor	L_r	95 μH
Resonant capacitor	C_r	20 nF
Switching frequency	f_s	115 KHz
Turn ratio	K	18:19
Transformer		EE65/32/27 PC40
Inductor		EE42/21/15 PC95
Controller		TMS320F28335

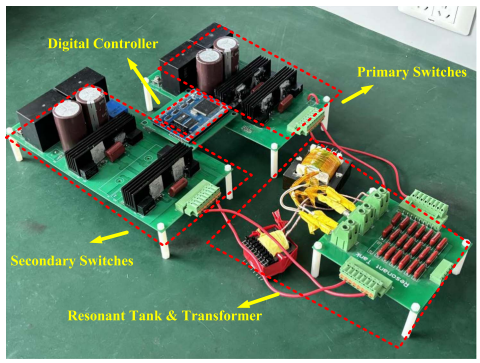

Fig. 8. Experiment setup.

V. EXPERIMENTAL VERIFICATION

A 500 VA experimental prototype of BSRC is built with the parameters given in Table II to verify the proposed CPDM method. The experimental setup is shown in Fig. 8.

A. Operating Waveforms

The operating and soft-switching waveforms are depicted in Fig. 10. The input voltage is $V_1 = 200$ V with $P = 1$, $M = 1$, and $D = 0.25$. The load resistance is $R_{\rm L} = 65\,\Omega$. The output voltage remains constant at $V_2 = 120$ V.

As shown in Fig. 9(a), the switching period is divided into three stages. In Stage 1, both v_{ab} and v_{cd} are square waves, generating sinusoid resonant current. Stage 2 corresponds to the resonant cycle. v_{ab} is regulated by duty cycle D using centrosymmetric PWM. The resonant current $i_{\rm r}$ is controlled and reaches zero at the end of the stage. Stage 3 features v_{ab} at zero level, while the resonant current remains sinusoidal, delivering power from the resonant tank to the load. Throughout the switching cycles, v_{cd} is modulated into a square wave with the resonant frequency.

The operation waveforms of S_1–S_8 are presented in Fig. 9(b), which are consistent with the operation principle analyzed in Section III, as shown in Fig. 3.

Specifically, the experiments with $N = 6$ and $M = 3$ are also conducted to verify the features of the proposed CPDM. The input voltage is $V_1 = 200$ V with $P = 2$, $M = 3$, and $D = 0.25$. The load resistance is $R_{\rm L} = 18\,\Omega$. The operation waveforms are given in Fig. 10(a) and (b). A same performance can be achieved with large N and M.

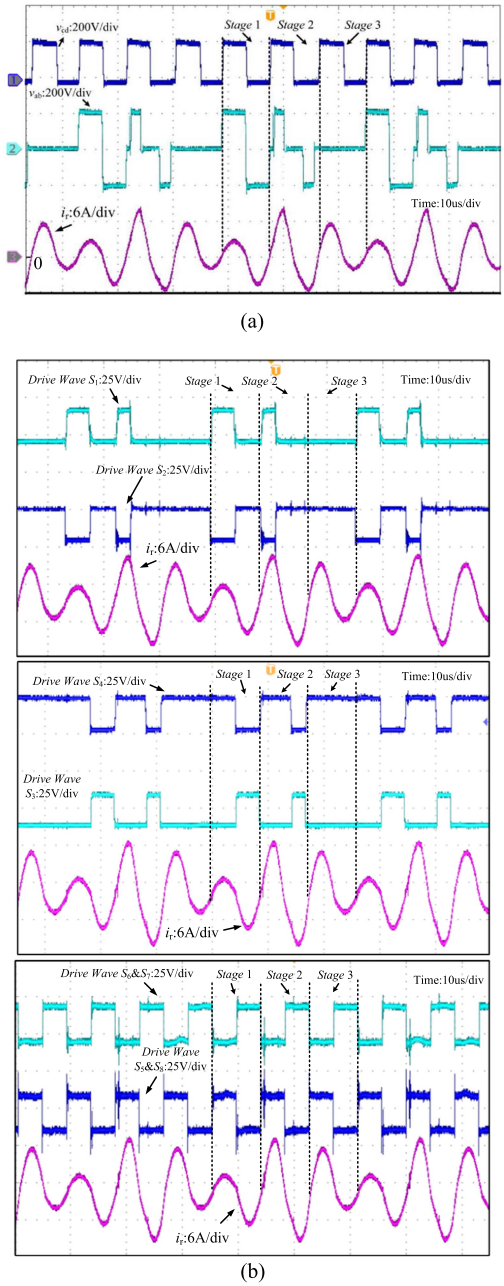

Fig. 9. Operation waveforms of CPDM with $P = 1$, $M = 1$ and $D = 0.25$. (a) Waveforms of terminal voltage and resonant current. (b) Operation waveforms of S_1–S_8.

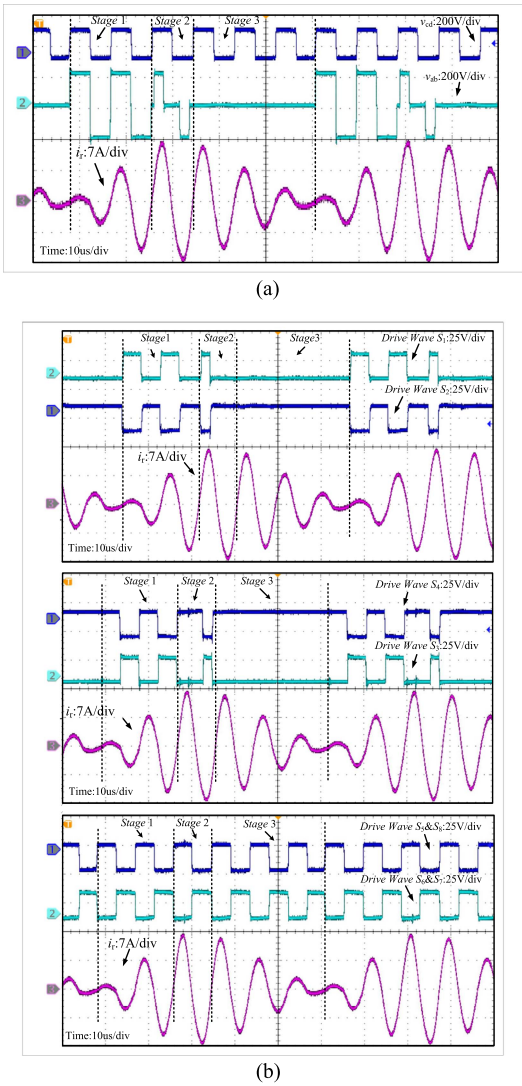

Fig. 10. Operation waveforms of CPDM with $P = 2$, $M = 3$ and $D = 0.25$. (a) Waveforms of terminal voltage and resonant current. (b) Operation waveforms of S_1–S_8.

In addition, the V_{ds} waveforms of the switches with $N = 3$ and $M = 1$ under heavy load ($R_L = 65\,\Omega$) and light load ($R_L = 120\,\Omega$) conditions are shown in Fig. 11. And the operation waveforms of S_1–S_8 with $N = 6$ and $M = 3$ under heavy load ($R_L = 18\,\Omega$) and light load ($R_L = 50\,\Omega$) are presented in Fig. 12. Under heavy load conditions, the resonant current is sufficient to flow through the antiparallel diodes, achieving ZVS-ON. Simultaneously, low-current turn-OFF is achieved. Since the current is near zero, ZCS-OFF is achieved. Under light load conditions, the resonant current is zero. Switches S_1 and S_2 achieve ZCS-ON and ZCS-OFF, while S_3 and S_4 achieve ZVS-ON and ZCS-OFF.

B. Measured Output Characteristics

Fig. 13 illustrates the measured output voltage V_2 as a function of different duty cycle D, with $P = 1$, $M = 0$, and $P = 2$, $M = 3$. When the duty cycle D is increased from 0 to 0.5, the output voltage linearly increases from 100 V to 200 V under condition of $P = 1$ and $M = 0$. And the output voltage rises from 66 V to 100 V for $P = 2$ and $M = 3$.

The waveforms of output voltage and resonant current for different duty cycle D are depicted in Figs. 14 and 15. With continuous voltage regulation capability, the proposed CPDM can achieve higher resolution compared to traditional PDM regardless of N and M.

Fig. 16 illustrates the experiment results of output voltage V_2 with $P = 1$, $M = 0$ and $P = 2$, $M = 3$ under different

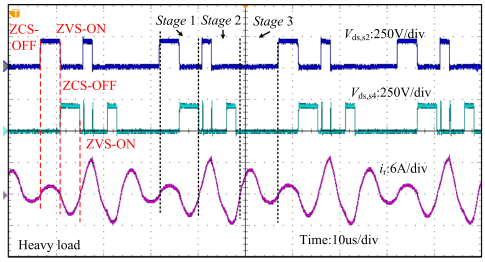

(a)

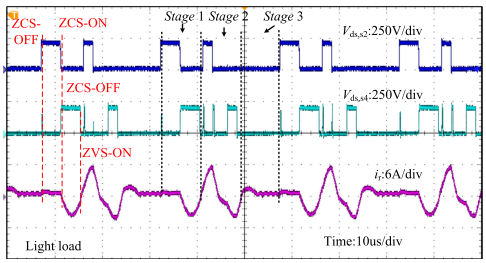

(b)

Fig. 11. Soft-switching waveforms under different load conditions with $P = 1$, $M = 1$, and $D = 0.25$. (a) Heavy load condition. (b) Light load condition.

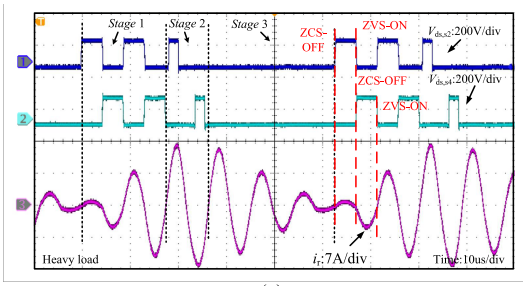

(a)

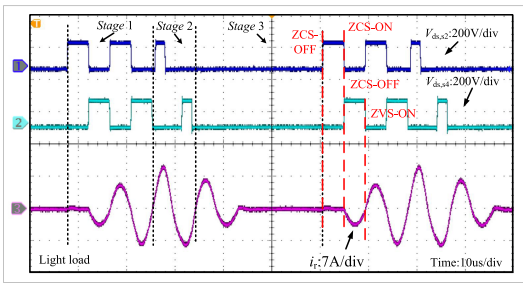

(b)

Fig. 12. Soft-switching waveforms under different load conditions with $P = 2$, $M = 3$, and $D = 0.25$. (a) Heavy load condition. (b) Light load condition.

delivered power P and duty cycle D. The output voltage remains nearly constant regardless of the delivered power.

The power transfer characteristic is shown in Fig. 17. When the load resistor is low, the converter operates in constant current mode, with the output voltage rising with the load. When the load resistor is high, the converter switches to constant voltage mode.

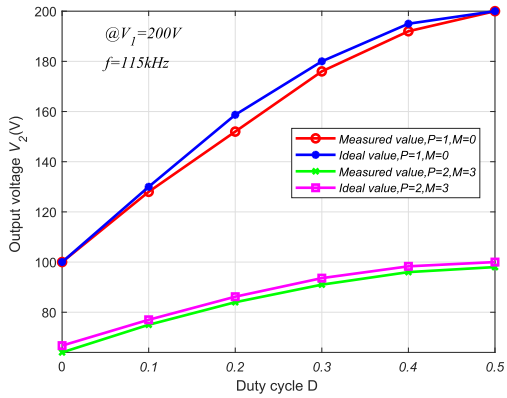

Fig. 13. Curves of output voltage V_2 versus duty cycle D.

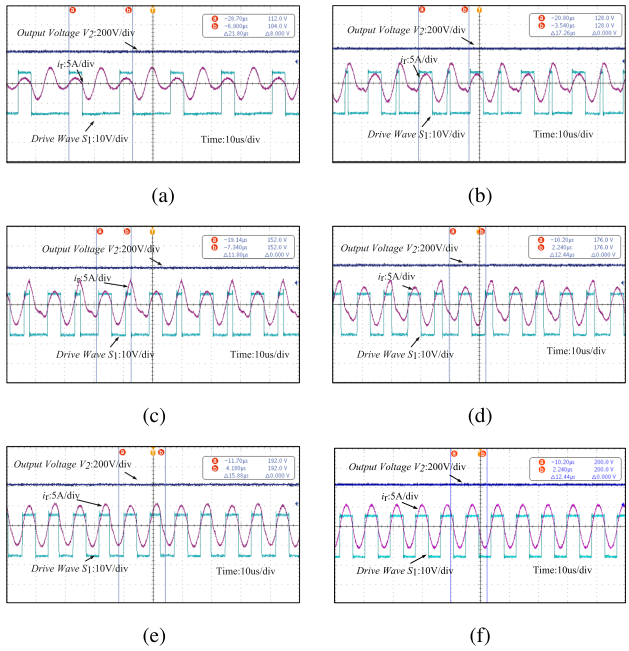

(a) (b) (c) (d) (e) (f)

Fig. 14. Waveforms of V_2 and resonant current i_r with different D. (a) $D = 0$. (b) $D = 0.1$. (c) $D = 0.2$. (d) $D = 0.3$. (e) $D = 0.4$. (f) $D = 0.5$.

C. Measured Efficiency

The measured efficiency are shown in Fig. 18, with V_2 fixed at 195 V, $D = 0.4$, $P = 1$, and $M = 0$. The delivered power is increased from 150 W to the peak value 500 W. The efficiency remains almost constant, ranging between 95% and 96%. The efficiency of traditional PDM are provided for comparison. To achieve similar output voltage resolution, the control cycle of PDM is 10 times that of CPDM, meaning CPDM contains only two resonant cycles while PDM contains 20 resonant cycles. This results in higher conduction loss with PDM, leading to lower efficiency compared to CPDM.

It is observed that under the same input conditions, the converter can achieve a maximum efficiency of 96% using the proposed PDM, representing a two-point improvement over traditional methods. Fig. 19 presents the power losses breakdown

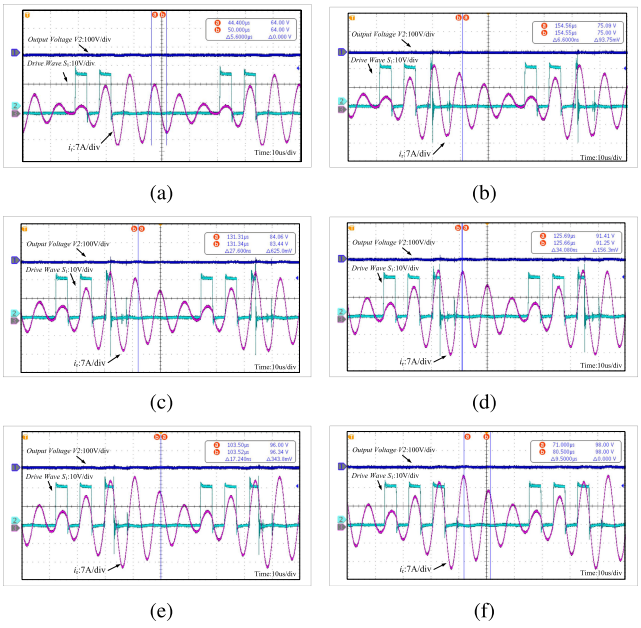

Fig. 15. Waveforms of V_2 and resonant current i_r with $P = 2$, $M = 3$ and different D. (a) $D = 0$. (b) $D = 0.1$. (c) $D = 0.2$. (d) $D = 0.3$. (e) $D = 0.4$. (f) $D = 0.5$.

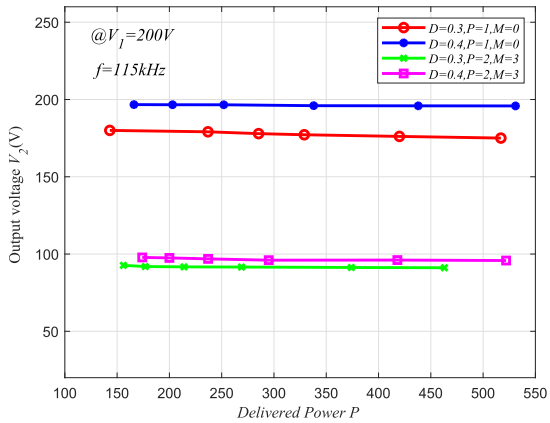

Fig. 16. Curves of output voltage versus delivered power.

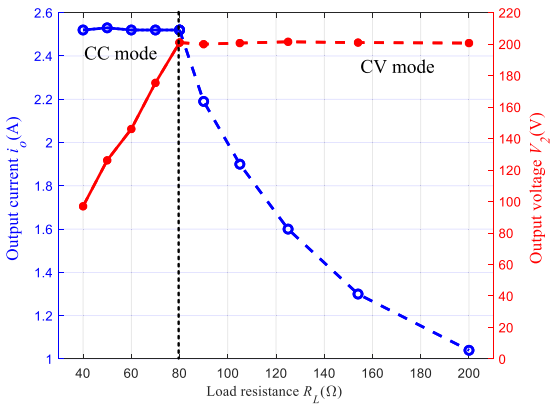

Fig. 17. Curves of output voltage and current versus load.

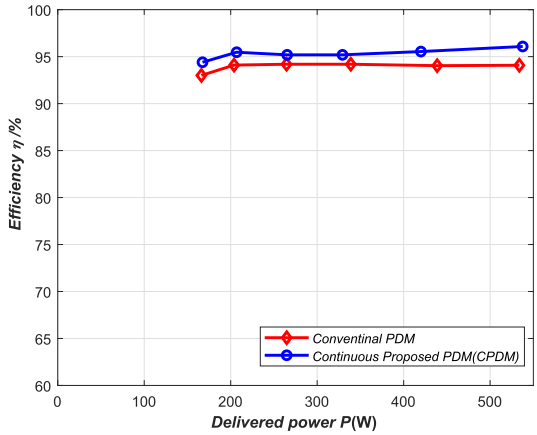

Fig. 18. Measured efficiency and power versus load resistance.

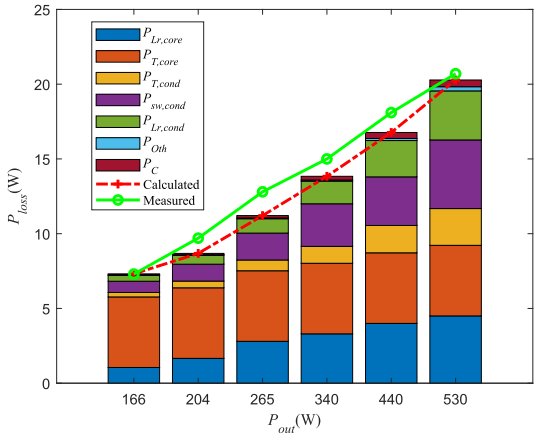

Fig. 19. Loss breakdown for $V_1 = 200\,\text{V}$, $D = 0.4$.

analysis. High efficiency can be achieved across a wide range, making it well-suited for battery charging applications.

VI. Conclusion

This article introduces a novel control method, named CPDM, for BSRC. Compared to traditional PDM, CPDM incorporates a hybrid modulation of PWM and PSM into one of the energy transfer switching cycles, enabling continuous and load-independent voltage regulation. The operation of the proposed CPDM is analyzed, the power characteristics and power losses are derived. CPDM achieves nearly full ZVZCS and minimal RMS of the resonant current, leading to high efficiency with almost constant values. Experimental results demonstrate high efficiency of up to 96% across a wide power range, validating the effectiveness of the proposed method.

Appendix

The converter losses can be calculated as follows.

1) Switch loss P_S

The switch loss $P_{\rm S}$ comprises the switching loss $P_{\rm sw}$ and the conduction loss $P_{\rm cond}$ of switches

$$P_S = P_{\rm sw} + P_{\rm cond}. \tag{50}$$

Due to the soft switching, the switching losses can be ignored. Only the conduction loss needs to be considered, which can be derived as

$$P_{\rm cond} = I_{\rm rms}^2(2r_{\rm d} + 2K^2 r_{\rm s}) \tag{51}$$

where $r_{\rm d}$ and $r_{\rm s}$ are the conduction resistances of the primary and secondary side switches, respectively. $I_{\rm rms}$ is the rms of resonance current.

2) Transformer loss $P_{\rm T}$

The loss of transformers, including core loss $P_{T,\rm core}$ and conduction loss $P_{T,\rm cond}$, can be expressed as

$$P_T = P_{T,\rm core} + P_{T,\rm cond}. \tag{52}$$

For a given frequency $f_{\rm r}$, the total loss of the iron core can be obtained as

$$P_{T,\rm core} = K_T f_{\rm r}^{\alpha_1} {B^{\beta_1}}_{T,\max} V_T \tag{53}$$

where α_1, β_1, V_T can be found in the product manual of the iron core material. $B_{T,\max}$ is the maximum magnetic flux density. Since $f_{\rm r}$ is fixed at a high value, constant, and minimal core loss can be achieved.

The conduction loss of the transformer is determined by the effective value of current $I_{\rm rms}$ and the ac resistance of the transformer, given by

$$P_{T,\rm cond} = {I^2}_{\rm rms} r_T \tag{54}$$

where r_T can be measured using an *LCR* meter.

3) Inductor loss $P_{\rm Lr}$

The losses of the inductor also include core loss and conduction loss, defined as

$$P_{Lr} = P_{Lr,\rm cond} + P_{Lr,\rm core}. \tag{55}$$

The core loss is obtained as

$$P_{Lr,\rm core} = K_{Lr} f_{\rm r}^{\alpha_2} {B^{\beta_2}}_{Lr,\max} V_{Lr}. \tag{56}$$

Similarly, the conduction loss can be calculated as

$$P_{Lr,\rm cond} = {I^2}_{\rm rms} r_{Lr} \tag{57}$$

where r_{Lr} is the ac resistance of the inductor, which can be measured using an *LCR* meter.

4) Capacitor loss and other loss

The capacitance loss P_C, caused by the equivalent resistance of the capacitor, is given by

$$P_C = {I^2}_{\rm rms} r_C \tag{58}$$

where $r_{\rm C}$ represents the equivalent series resistance of the capacitor, which can be obtained from the data manual. Other losses $P_{\rm Oth}$ can be obtained as

$$P_{\rm Oth} = {I^2}_{\rm rms} r_{\rm oth} \tag{59}$$

where $\rm r_{oth}$ represents other resistances of the wires and the circuits.

REFERENCES

[1] M. Jahnes, L. Zhou, M. Eull, W. Wang, and M. Preindl, "Design of a 22-kW transformerless EV charger with V2G capabilities and peak 99.5% efficiency," *IEEE Trans. Ind. Electron.*, vol. 70, no. 6, pp. 5856–5871, Jun. 2023.

[2] M. Yilmaz and P. T. Krein, "Review of battery charger topologies charging power levels and infrastructure for plug-in electric and hybrid vehicles," *IEEE Trans. Power Electron.*, vol. 28, no. 5, pp. 2151–2169, May 2013.

[3] T. Luo et al., "A full-iteration optimal design methodology of CLLC converter with minimized RMS current," *IEEE Trans. Power Electron.*, vol. 39, no. 10, pp. 11916–11930, Oct. 2024.

[4] T. Yuan, F. Jin, and Q. Li, "Analysis and comparison of integrated planar transformers for 22-kW on-board chargers," *IEEE Trans. Power Electron.*, vol. 39, no. 9, pp. 11368–11385, Sep. 2024.

[5] Z. Fang, Z. Wei, Z. Huang, and F. Liu, "Onboard energy storage system based on interleaved high-conversion-ratio quasi-resonant converter with small characteristic impedance," *IEEE Trans. Veh. Tech.*, vol. 70, no. 5, pp. 4238–4251, May 2021.

[6] F. Liu, X. Ruan, and Y. Jiang, "Resonant peak suppression approaches for improving the dynamic performance of DCX-LLC resonant converter based two-stage DC–DC converter," *IEEE Trans. Ind. Electron.*, vol. 70, no. 6, pp. 5685–5695, Jun. 2023.

[7] T. Chen, R. Yu, and A. Q. Huang, "A bidirectional isolated dual-phase-shift variable-frequency series resonant dual-active-bridge GaN AC–DC converter," *IEEE Trans. Ind. Electron.*, vol. 70, no. 4, pp. 3315–3325, Apr. 2023.

[8] J. Deng, S. Li, S. Hu, C. C. Mi, and R. Ma, "Design methodology of LLC resonant converters for electric vehicle battery chargers," *IEEE Trans. Vehi. Tech.*, vol. 63, no. 4, pp. 1581–1592, May 2014.

[9] Y. Zuo, X. Pan, and C. Wang, "A reconfigurable bidirectional isolated LLC resonant converter for ultra-wide voltage-gain range applications," *IEEE Trans. Ind. Electron.*, vol. 69, no. 6, pp. 5713–5723, Jun. 2022.

[10] Z. Fang, T. Cai, S. Duan, and C. Chen, "Optimal design methodology for LLC resonant converter in battery charging applications based on time-weighted average efficiency," *IEEE Trans. Power Electron.*, vol. 30, no. 10, pp. 5469–5483, Oct. 2015.

[11] H. Wu, S. Ding, K. Sun, L. Zhang, Y. Li, and Y. Xing, "Bidirectional soft-switching series-resonant converter with simple PWM control and load-independent voltage-gain characteristics for energy storage system in DC microgrids," *IEEE J. Emerg. Sel. Topics Power Electron.*, vol. 5, no. 3, pp. 995–1007, Mar. 2017.

[12] R.-L. Lin and L.-H. Huang, "Efficiency improvement on LLC resonant converter using integrated LCLC resonant transformer," *IEEE Trans. Ind. Appl.*, vol. 54, no. 2, pp. 1756–1764, Mar./Apr. 2018.

[13] Y. Wei and N. Author_Id, "LLC and LCL-T resonant tanks based topology for battery charger application," *CPSS Trans. Power Electron. Appl.*, vol. 6, no. 4, pp. 263–275, Dec. 2021.

[14] H. Wu, X. Zhan, and Y. Xing, "Interleaved LLC resonant converter with hybrid rectifier and variable-frequency plus phase-shift control for wide output voltage range applications," *IEEE Trans. Power Electron.*, vol. 32, no. 5, pp. 4246–4257, May 2017.

[15] Z. Fang, H. Yue, Z. Wei, Z. Zhang, and Z. Huang, "A control-free series resonant converter for battery charging with automatic CC-to-CV profile and whole-process high efficiency," *IEEE Trans. Power Electron.*, vol. 38, no. 7, pp. 8666–8675, Jul. 2023.

[16] L. Corradini, D. Seltzer, D. D. Bloomquist, R. Zane, D. Maksimović, and B. Jacobson, "Zero voltage switching technique for bidirectional DC/DC converters," *IEEE Trans. Power Electron.*, vol. 29, no. 4, pp. 1585–1594, Apr. 2014.

[17] H.-P. Park, M. Kim, and J. Jung, "Investigation of zero voltage switching capability for bidirectional series resonant converter using phase-shift modulation," *IEEE Trans. Power Electron.*, vol. 34, no. 9, pp. 8842–8858, Sep. 2019.

[18] B. Zhao, Q. Song, and W. Liu, "Power characterization of isolated bidirectional dual-active-bridge DC–DC converter with dual-phase-shift control," *IEEE Trans. Power Electron.*, vol. 27, no. 9, pp. 4172–4176, Sep. 2012.

[19] G. Xu, J. Tang, L. Zhang, W. Xiong, Y. Sun, and M. Su, "A hybrid extended phase shift modulation strategy for DAB converter with DC blocking capacitor to extend ZVS range and reduce RMS current," *IEEE Trans. Emerg. Sel. Topics Power Electron.*, vol. 10, no. 5, pp. 6192–6207, Oct. 2022.

[20] L. Deng, G. Zhou, Q. Bi, and N. Xu, "Online reactive power minimization and soft switching algorithm for triple-phase-shift modulated dual active bridge converter," *IEEE Trans. Ind. Electron.*, vol. 70, no. 3, pp. 2543–2555, Mar. 2023.

[21] W. L. Malan, D. M. Vilathgamuwa, and G. R. Walker, "Modeling and control of a resonant dual active bridge with a tuned CLLC network," *IEEE Trans. Power Electron.*, vol. 31, no. 10, pp. 7297–7310, Oct. 2016.
[22] C. Sun et al., "Generalized multiphase-shift transient modulation for dual-active-bridge series-resonant converter," *IEEE Trans. Power Electron.*, vol. 38, no. 7, pp. 8291–8309, Jul. 2023.
[23] J. Liu, Y. Ai, S. Chen, Z. Zhang, and Y. Shi, "A hybrid pulse frequency modulation control strategy for L-LLC resonant converter," *IEEE Trans. Emerg. Sel. Topics Power Electron.*, vol. 10, no. 6, pp. 6960–6972, Dec. 2022.
[24] W. Chen, P. Rong, and Z. Lu, "Snubberless bidirectional DC-DC converter with new CLLC resonant tank featuring minimized switching loss," *IEEE Trans. Ind. Electron.*, vol. 57, no. 9, pp. 3075–3086, Sep. 2010.
[25] L. Corradini, D. Seltzer, D. Bloomquist, R. Zane, D. Maksimović, and B. Jacobson, "Minimum current operation of bidirectional dual-bridge series resonant DC-DC converters," *IEEE Trans. Power Electron.*, vol. 27, no. 7, pp. 3266–3276, Jul. 2012.
[26] F. Wu, K. Wang, and S. Luo, "Hybrid-three-level current-fed series-resonant isolated DC-DC converter and its optimization modulation strategy," *IEEE Trans. Power Electron.*, vol. 37, no. 1, pp. 196–205, Jan. 2022.
[27] W. Han and L. Corradini, "Wide-range ZVS control technique for bidirectional dual-bridge series resonant DC-DC converters," *IEEE Trans. Power Electron.*, vol. 34, no. 10, pp. 10256–10269, Oct. 2019.
[28] M. Yaqoob, K. H. Loo, and Y. M. Lai, "A four-degrees-of-freedom modulation strategy for dual-active-bridge series-resonant converter designed for total loss minimization," *IEEE Trans. Power Electron.*, vol. 34, no. 2, pp. 1065–1081, Feb. 2019.
[29] T. Zhu, F. Zhuo, F. Zhao, F. Wang, Y. Hao, and T. Zhao, "Optimization of extended phase-shift control for full-bridge CLLC resonant converter with improved light-load efficiency," *IEEE Trans. Power Electron.*, vol. 35, no. 10, pp. 11129–11142, Oct. 2020.
[30] D. Bourner, "Bidirectional DC-DC converter systems: Sustaining power component design methodology to achieve critical power conditioning," *IEEE Power Electron. Mag.*, vol. 5, no. 2, pp. 66–71, Jun. 2018.
[31] Z. Fang, H. Dong, H. Sun, F. Xie, and Z. Huang, "Intermittent sinusoidal modulation of bidirectional series resonant converter with zero current switching, linear current controllability, and load-independent efficiency," *IEEE Trans. Power Electron.*, vol. 37, no. 10, pp. 11725–11738, Oct. 2022.
[32] H. Li, J. Fang, S. Chen, K. Wang, and Y. Tang, "Pulse density modulation for maximum efficiency point tracking of wireless power transfer systems,," *IEEE Trans. Power Electron.*, vol. 33, no. 6, pp. 5492–5501, Jun. 2018.
[33] H. Fujita and H. Akagi, "Control and performance of a pulse-density modulated series-resonant inverter for corona discharge processes," *IEEE Trans. Ind. Appl.*, vol. 35, no. 3, pp. 621–627, May/Jun. 1999.
[34] V. Esteve et al., "Enhanced pulse-density-modulated power control for high-frequency induction heating inverters," *IEEE Trans. Ind. Electron.*, vol. 62, no. 11, pp. 6905–6914, Nov. 2015.
[35] X. Sheng, L. Shi, and M. Fan, "An improved pulse density modulation of high-frequency inverter in ICPT system," *IEEE Trans. Ind. Electron.*, vol. 68, no. 9, pp. 8017–8027, Sep. 2021.

Zhijian Fang (Member, IEEE) received the B.S. and Ph.D. degrees in electrical engineering and automation from the Huazhong University of Science and Technology, Wuhan, China, in 2010 and 2015, respectively.

Since 2018, he has been a Professor with the School of Automation, China University of Geosciences, Wuhan, China. His research interests include high performance dc–dc converter, battery charger, renewable energy applications, and wireless power transfer.

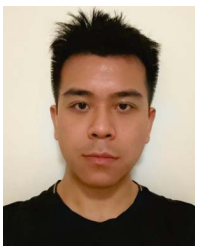

Shizhao Liu received the bachelor's degree in electrical engineering and automation in 2021 from Wuhan Textile University, Wuhan, China, where he is currently working toward the master's degree in electronic and information engineering.

His research focuses on power electronic converter and its control method.

Rui Li received the Ph.D. degree in electrical engineering from the Huazhong University of Science and Technology (HUST), Wuhan, China, in 2014.

He is currently a Research Fellow with the Wuhan Second Ship Design and Research Institute. His research interests include multiphase motor control systems, low-noise motor design, and high-efficiency high-power-density electrical energy conversion.

Yunfei Zhao received the B.S. degree in automation in 2023 from the China University of Geosciences, Wuhan, China, where he is currently working toward the M.S. degree in electronic information.

His research interests include the balance of the three-phase four-wire power supply network.

Li Fang received the Ph.D. degree in electrical engineering from Wuhan University, Wuhan, China, in 2022.

He is currently a Power Electronics Engineer with Wuhan Second Ship Design and Research Institute, Wuhan, China. His research interests include power conversion system, ac–dc converter, and wireless power transfer.

Han Cao received the Ph.D. degree in electrical engineering from the Institute of Electrical Engineering, Chinese Academy of Sciences, Beijing, China, in 2022.

He is currently an Electrical Engineer with Wuhan Second Ship Design and Research Institute, Wuhan, China. His current research interests include power device modeling and high-density converter designs.

Junhao Luo (Member, IEEE) received the B.S. degree in electrical engineering from Wuhan University, Wuhan, China, in 2015, the M.S. degree in electrical engineering from Wuhan University, Wuhan, China, in 2018, and the Ph.D. degree in electrical engineering from Northeastern University, Boston, MA, USA, in 2024.

He is currently a Senior Product Applications Engineer with Analog Devices Inc., Wilmington, MA, USA. His areas of interest are power electronics, design and digital control of power converters.